ADVANCED MATERIALS
www.advmat.de

Single-Crystal Structure Determination of Superconducting $La_4Ni_3O_{10-\delta}$ under High Pressure

Feiyu Li, Yinqiao Hao, Ning Guo, Donghan Jia, Jie Dou, Di Peng, Gongting Zhang, Lingfeng Xiao, Jian Zhang, Wenju Zhou, Yehua Huang, Xinyu Wang, Zhenyuan Guo, Mohamed Mezouar, João Elias F. S. Rodrigues, Jun Luo, Jie Yang, Qiaoshi Zeng, Rui Zhou,* Huiyang Gou,* Qiang Zheng,* Guangtao Liu,* and Junjie Zhang**

Ruddlesden-Popper nickelates have attracted enormous attention since the discovery of high-temperature superconductivity in bilayer $La_3Ni_2O_7$ under high pressure. However, the crystal structure under high pressure remains elusive due to the lack of single crystal diffraction data. Here, high-pressure superconductivity with a superconducting onset temperature approaching 30K and a zero-resistance state at 7K at 53.8 GPa is reported in high-quality single crystals of trilayer $La_4Ni_3O_{10-\delta}$ grown at ambient pressure. A cascade of structural transitions from $P2_1/a$ at 5.7 GPa to *Bmab* at 11.0 GPa and to $I4/mmm$ at 16.6 GPa is unambiguously determined via synchrotron X-ray single crystal diffraction, revealing a correlation between the tetragonal $I4/mmm$ and the emergence of superconductivity. These results not only demonstrate that ambient-pressure grown nickelate single crystals can superconduct under high pressure but also reveal an intermediate structure that was not reported under high pressure, providing new insights into the physics of nickelate superconductivity.

1. Introduction

The mechanism of high-temperature (T_c) superconductivity remains a major challenge.[1,2] Design and discovery of non-copper transition metal oxide high-T_c superconductors are expected to provide new materials platforms and new insights for unlocking the above mystery.[3] Nickelates have been searched for superconductivity since 1983.[4] After a 36-year quest,[5–7] superconductivity was finally realized in the square-planar infinite-layer $Nd_{0.8}Sr_{0.2}NiO_2$[8] thin films, stimulating world-wide interest in nickelates.[9–15] To date, superconductivity has been reported in thin films of infinite-layer $R_{1-x}A_xNiO_2$ (R = La, Pr, Nd, Sm; A = Sr, Ca, Eu)[8,16–22] and

---

F. Li, G. Zhang, J. Zhang, J. Zhang
Institute of Crystal Materials
State Key Laboratory of Crystal Materials
Shandong University
Jinan, Shandong 250100, China
E-mail: junjie@sdu.edu.cn

Y. Hao, L. Xiao, G. Liu
State Key Laboratory of Superhard
Materials and International Center of Computational Method & Software
College of Physics
Jilin University
Changchun 130012, China
E-mail: liuguangtao@jlu.edu.cn

N. Guo, Q. Zheng
CAS Key Laboratory of Standardization and Measurement for Nanotechnology
CAS Center for Excellence in Nanoscience
National Center for Nanoscience and Technology
Beijing 100190, China
E-mail: zhengq@nanoctr.cn

D. Jia, W. Zhou, Y. Huang, X. Wang, Z. Guo, H. Gou
Center for High Pressure Science and Technology Advanced Research (HPSTAR)
Beijing 100193, China
E-mail: huiyang.gou@hpstar.ac.cn

J. Dou, J. Luo, J. Yang, R. Zhou
Beijing National Laboratory for Condensed Matter Physics and Institute of Physics
Chinese Academy of Sciences
Beijing 100190, China
E-mail: rzhou@iphy.ac.cn

J. Dou, R. Zhou
School of Physical Sciences
University of Chinese Academy of Sciences
Beijing 100190, China

D. Peng, Q. Zeng
Center for High Pressure Science and Technology Advanced Research
Shanghai 201203, China

D. Peng, Q. Zeng
Shanghai Key Laboratory of Material Frontiers Research in Extreme Environments (MFree)
Shanghai Advanced Research in Physical Sciences (SHARPS)
Shanghai 201203, China
E-mail: zengqs@hpstar.ac.cn

M. Mezouar, J. Elias F. S. Rodrigues
European Synchrotron Radiation Facility (ESRF)
Grenoble 38000, France

The ORCID identification number(s) for the author(s) of this article can be found under https://doi.org/10.1002/adma.202507365

DOI: 10.1002/adma.202507365

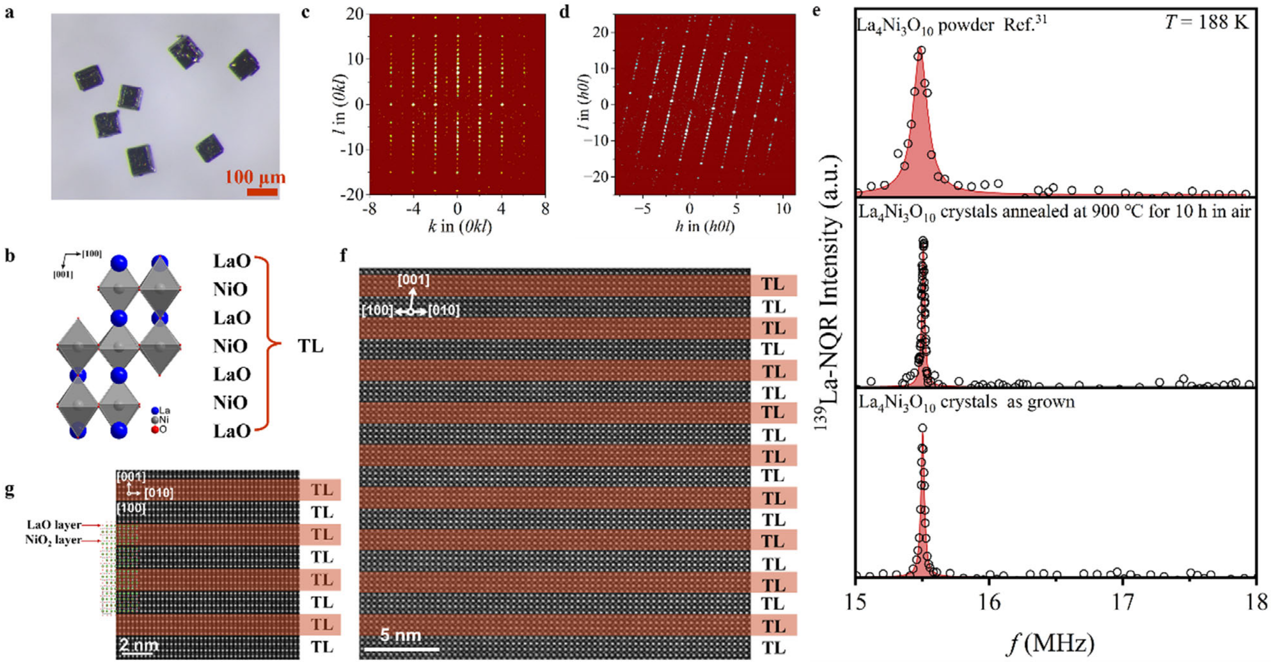

Figure 1. Crystallinity of $La_4Ni_3O_{10-\delta}$ single crystals grown at ambient pressure. a) Photograph of typical as-grown $La_4Ni_3O_{10-\delta}$ single crystals. b) Structural model of trilayer $La_4Ni_3O_{10-\delta}$ with LaO layers, NiO_2 layers, and trilayer (TL) labeled. c) Reconstructed (*0kl*) plane from single crystal X-ray diffraction data collected at 298K. d) Reconstructed (*h0l*) plane from single crystal X-ray diffraction data collected at 298 K. e) ^{139}La (2) NQR spectra corresponding to the $\pm5/2\leftrightarrow\pm7/2$ transition in $La_4Ni_3O_{10-\delta}$ crystals at 188K. The solid lines represent the Lorentz fit. f) A wide-range high-angle annular dark-field (HAADF)-STEM image along [110] with trilayer indicated. g) A typical atomic-scale HAADF-STEM image along [100] projection with overlaid crystal structure and trilayer indicated.

quintuple-layer $Nd_6Ni_5O_{12}$.[23,24] However, the T_c of these nickelates are still below 40K,[20] and superconductivity has been limited to thin films.[25–27] The second family of nickelate superconductors is hybrid Ruddlesden-Popper (R-P) phases with octahedral environments of Ni, represented by the bilayer $La_3Ni_2O_7$ with T_c of ≈80K.[28] Superconductivity has been reported in bulk samples under high pressures[28–43] and thin films at ambient pressure.[44,45] Various theoretical models have been proposed to understand the nature of high-T_c superconductivity.[28,46–53] Besides bilayer $La_3Ni_2O_7$, superconductivity was also reported in bilayer $La_2PrNi_2O_7$,[31] trilayer $R_4Ni_3O_{10}$ (R = La, Pr),[32–35] and hybrid R-P $La_2NiO_4{\cdot}La_3Ni_2O_7$.[36,37] Recently, by introducing chemical pressure, the T_c of nickelates have been increased to the 90K range with a zero-resistance state approaching the boiling point of liquid nitrogen (77K).[38]

Despite significant progress in the past years, the crystal structure of hybrid R-P nickelates under high pressure remains elusive. Synchrotron X-ray powder diffraction has been utilized to study the structural evolution of hybrid R-P nickelates as a function of pressure, and phase transitions have been reported in $La_3Ni_2O_7$ (*Amam* → *Fmmm*,[28] *Amam* → *I4/mmm*[39]), $La_2PrNi_2O_7$ (*Amam* → *I4/mmm*[31]), $La_4Ni_3O_{10}$ ($P2_1/a$ → *I4/mmm*[32,33,54]), $Pr_4Ni_3O_{10}$ ($P2_1/a$ → *I4/mmm*[34]), and $La_2NiO_4{\cdot}La_3Ni_2O_7$ (*Cmmm* → *P4/mmm*[37]) at room temperature. In sharp contrast, the absence of structural transitions was also reported in $La_3Ni_2O_7$[40] and $Pr_4Ni_3O_{10}$[55] under high pressure. Single-crystal diffraction is demanded for resolving the above controversies. To date, there is only one high-pressure single-crystal diffraction report on nickelates. Specifically, Zhu et al reported *I4/mmm* structure in $La_4Ni_3O_{10}$ at 19.5 GPa at room temperature by combining single-crystal X-ray diffraction and neutron diffraction;[32] however, how the crystal structure of $La_4Ni_3O_{10}$ evolves as a function of pressure remains an open question. No high-pressure single-crystal diffraction study has been reported on $La_3Ni_2O_7$, $La_2PrNi_2O_7$, $Pr_4Ni_3O_{10,}$ and $La_2NiO_4{\cdot}La_3Ni_2O_7$. Furthermore, crystal structure determination of the superconducting phase at low temperature and high pressure using single-crystal diffraction is still lacking for all nickelate superconductors.

In order to obtain superconductivity in nickelate single crystals, two "high pressure" conditions were previously required, i.e., high oxygen pressure for floating zone crystal growth (e.g., 10–15 bar for $La_3Ni_2O_7$[41] and 18–30 bar for $La_4Ni_3O_{10}$[41]) and high pressure (>14 GPa) for inducing superconductivity[18,32–34,42] Overcoming the two high-pressure conditions remains an urgent task.[42] Recently, we reported the world's first single crystal growth of hybrid R-P nickelates at ambient pressure, including trilayer $La_4Ni_3O_{10-\delta}$[43] and hybrid $La_2NiO_4{\cdot}La_3Ni_2O_7$,[36] overcoming the first high-pressure barrier. This newly developed ambient-pressure flux growth method makes it easy to access high quality single crystals with no need of high oxygen pressure and expensive floating zone furnaces. Whether the ambient-pressure grown single crystals of $La_4Ni_3O_{10-\delta}$ superconduct under high pressure remains an important open question.

In this contribution, we report superconductivity in ambient-pressure flux grown single crystals of $La_4Ni_3O_{10-\delta}$.

Single crystal X-ray diffraction (SC-XRD), nuclear quadrupole resonance (NQR) and scanning transmission electron microscopy (STEM) measurements showed that the as-grown $La_4Ni_3O_{10-\delta}$ single crystals are of high quality without stacking faults within our resolution. The high-pressure resistance measurements show that the metal-to-metal transition at ≈ 135K observed at ambient pressure was suppressed under high pressure, and superconductivity was observed with the maximum onset temperature of ≈30K and the maximum zero-resistance temperature of 7K. Furthermore, synchrotron SC-XRD under high pressure revealed that $La_4Ni_3O_{10-\delta}$ undergoes a series of structural phase transitions from ambient-pressure $P2_1/a$ to intermediate-pressure *Bmab* and finally to the tetragonal *I*4/*mmm*. Among them, the intermediate-pressure *Bmab* is reported for the first time.

2. Results and Discussion

2.1. Crystallinity of As-Grown $La_4Ni_3O_{10-\delta}$ Single Crystals

Figure 1a shows a photograph of typical as-grown single crystals of $La_4Ni_3O_{10-\delta}$. Figure S1 (Supporting Information) shows the in-house PXRD data and Rietveld refinement of pulverized as-grown single crystals using $P2_1/a$. The refinement converged to R_{wp} = 3.87%, R_{exp} = 2.98%, and GOF = 1.3. The obtained lattice parameters for $La_4Ni_3O_{10-\delta}$ are a = 5.4185(1) Å, b = 5.4676(1) Å, c = 14.2290(2) Å, and β = 100.7247(7)°, consistent with previous reports.[41,43] It is worth noting that Rietveld refinement reveals a small amount of impurity phase which belongs to $La_3Ni_2O_7$ (≈4 wt.%, $La_3Ni_2O_7$ single crystals were found in SC-XRD). Similar phenomena have been reported in the flux growth of $La_2NiO_4 \cdot La_3Ni_2O_7$ single crystals.[36]

We characterized the crystalline quality of as-grown $La_4Ni_3O_{10-\delta}$ single crystals using SC-XRD, NQR, and STEM. Figure 1b shows the structural model of $La_4Ni_3O_{10-\delta}$ in the *ac* plane (space group $P2_1/a$). Figure 1c,d shows the reconstructed (*0kl*) and (*h0l*) planes from a total of 2971 frames from SC-XRD data collected at 298K. The sharp diffraction peaks and neat distribution of reflections demonstrate high crystallinity of the as-grown $La_4Ni_3O_{10-\delta}$ single crystals. We then investigated possible intergrowth of R-P phases in $La_4Ni_3O_{10-\delta}$ single crystals using NQR as a sensitive global probe. As can be seen in Figure 1e, the NQR spectra of $La_4Ni_3O_{10-\delta}$ at 188K show a single resonant peak, $La^{4310}(2)$, indicating high purity without intergrowth. Notably, the linewidth of $La_4Ni_3O_{10-\delta}$ single crystals is six times narrower than that of polycrystalline samples,[31] indicating a significant improvement in crystallinity. Real-space imaging of the structure of as-grown $La_4Ni_3O_{10-\delta}$ single crystals was performed using STEM. Figure 1f shows a wide-range high-angle annular dark-field (HAADF)-STEM image along [110] with trilayer indicated, and Figure 1g shows a typical atomic-scale HAADF-STEM image along [100] projection with trilayer indicated. Clearly, $La_4Ni_3O_{10-\delta}$ single crystals grown at ambient pressure maintain a clean stacking of trilayer perovskite layers alternating with rock-salt layers in the long-range order (see Figures S2–S5, Supporting Information for more HAADF-STEM images). No hybrid R-P phases such as $La_2NiO_4 \cdot La_4Ni_3O_{10}$[56–58] or $La_2NiO_4 \cdot La_3Ni_2O_7$,[36] or short-range intergrowth were found.

2.2. Physical Properties of Pulverized $La_4Ni_3O_{10-\delta}$ Single Crystals at Ambient Pressure

Resistivity and magnetic susceptibility were measured at ambient pressure to further verify the high quality of our samples. The as-grown single crystals with dimensions of ≈100 µm are too small to put four leads on so we measured resistivity using the conventional four-probe method on pressed polycrystalline pellets by pulverizing single crystals. The pellets were annealed at 900 °C in air for 10 h to increase density and reduce oxygen defects. Powder X-ray diffraction confirmed no structural change after annealing (Figure S6, Supporting Information). Figure S7 (Supporting Information) shows the resistivity as a function of temperature. A clear metal-to-metal transition at ≈135K is observed, consistent with previous reports.[32,43] The magnetic susceptibility (Figure S8, Supporting Information) decreases as a function of temperature and shows an anomaly at ≈135K, corresponding to the formation of intertwined charge and spin density waves.[59] Below ≈80K, an upturn in magnetic susceptibility is observed. No obvious magnetic field dependence of the transition at ≈ 135K was found in both resistivity and magnetic susceptibility measurements (Figures S7 and S8, Supporting Information).

2.3. Superconductivity in Pressurized $La_4Ni_3O_{10-\delta}$ Single Crystals

Figure 2a shows the temperature dependent resistance of Crystal #3 at pressures ranging from 6.1 to 66.8 GPa using helium as pressure transmitting medium (PTM). Superconductivity was observed above 44.6 GPa with the maximum T_c^{onset} of 29K and the maximum T_c^{zero} of 7K at 53.8 GPa, as shown in Figure 2b. Figure 2c shows the field dependence of the resistance of Crystal #3 at 53.8 GPa. Notably, the T_c is significantly suppressed with the increasing of magnetic field up to 7 T. By utilizing the criteria of 90% of the normal state resistance values, we extrapolated the value of upper critical magnetic field $\mu_0H_{c2}(T)$ at 53.8 GPa and zero temperature to be 32.5 T (Figure 2d), and calculated the zero-temperature coherence length $\xi(0)$ to be 3.18 nm using the Ginzburg-Landau (GL) model. Figure S9 (Supporting Information) shows the field dependence of the resistance of Crystal #3 at 60.4 GPa and 66.8 GPa, and the estimated values of upper critical magnetic field $\mu_0H_{c2}(T)$ at 60.4 GPa and 66.8 GPa are 34 and 27.5 T, respectively (Figure 2d). These values are consistent with Zhu et al.[32] Moreover, our thermogravimetric analysis (TGA) measurements of $La_4Ni_3O_{10-\delta}$ polycrystalline powders annealed using the same conditions as Crystal #3 (annealed at 600 °C under pO_2 = 1.5 bar for 10 days) result in an oxygen content of 10.26(1) and 10.25(1) from two different batches (Figure S10a,b, Supporting Information). These results indicate that hole doped $La_4Ni_3O_{10}$ can support superconductivity under high pressure.

Besides helium, we also performed high-pressure transport measurements using KBr as PTM. Figure 2e shows the temperature-dependent resistances of Crystal #1 under pressure ranging from 4.8 to 77.9 GPa. At 4.8 GPa, the known metal-to-metal transition (MMT) is clearly seen, and the transition temperature (T_{MMT}) is ≈107.5K, much lower than that at ambient pressure. As the pressure increases, the resistance decreases significantly, and the MMT gradually disappears. When the pressure increases to 13.6 GPa, the MMT is barely observed, and

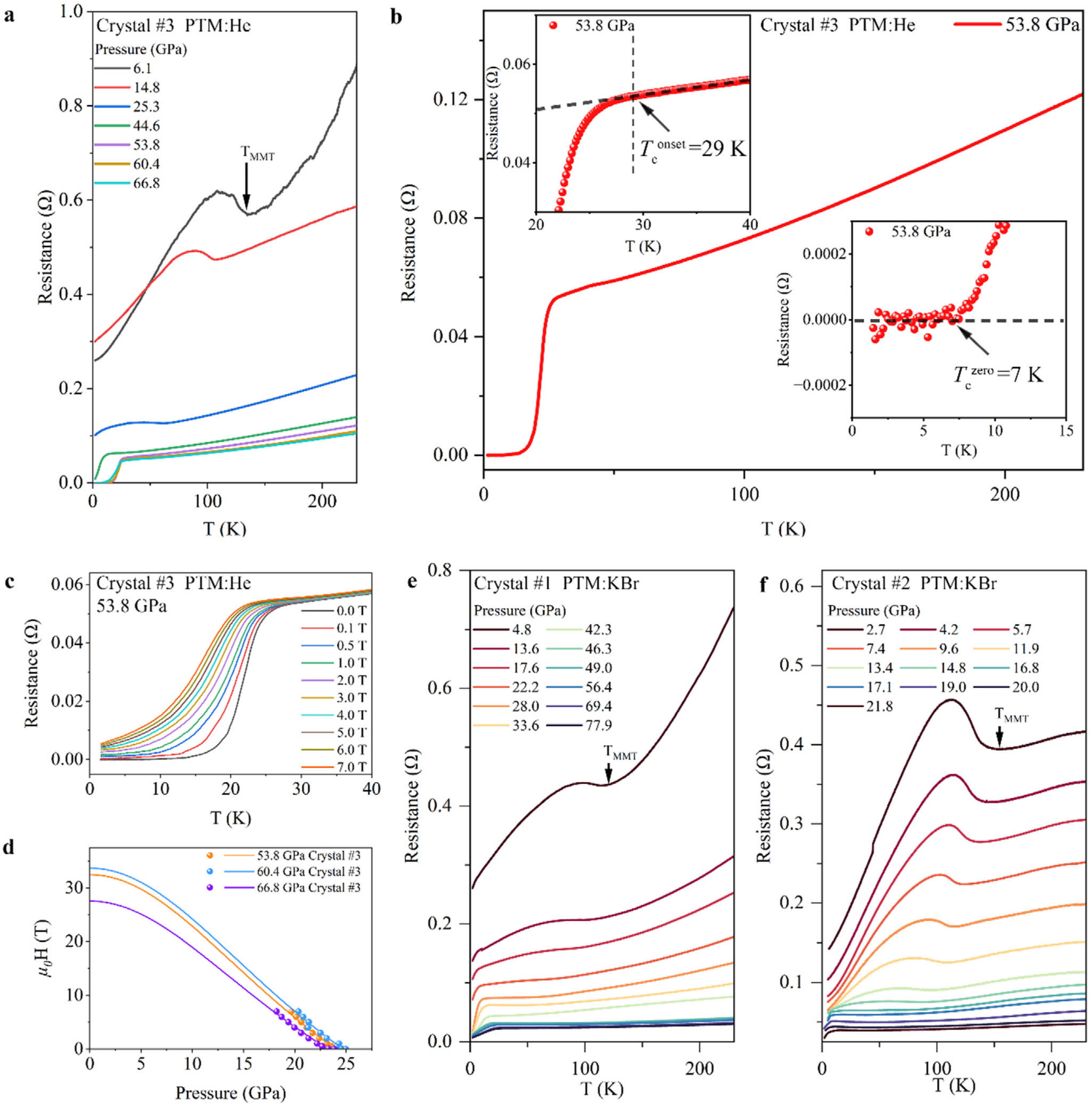

Figure 2. Superconductivity in $La_4Ni_3O_{10-\delta}$ single crystals under high pressures. a) Temperature dependent resistance of Crystal #3 at 6.1-66.8 GPa using helium as pressure transmitting medium (PTM). b) Temperature dependent resistance of Crystal #3 at 53.8 GPa using helium as PTM. The insets show the zoom-in region around T_c^{onset} and T_c^{zero}. c) Magnetic field dependence of electrical resistance at 53.8 GPa for Crystal #3. d) Upper critical fields extracted using the normal-state resistance values at 90% of the resistance of T_c^{onset}. Note solid spheres represent data and solid lines show the fit using a Ginzburg-Landau (GL) model $H_{c2}(T) = H_{c2}(0)\ [(1-t)^2/(1+t)^2]$, where $t = T/T_c$. e) Temperature dependent resistance of Crystal #1 at 4.8–77.9 GPa using KBr as PTM. f) Temperature dependent resistance of Crystal #2 at 2.7-21.8 GPa using KBr as PTM. Note Crystal #1 and Crystal #2 were annealed at 900 °C in air for 10 h, and Crystal #3 was annealed at 600 °C under $pO_2 = 1.5$ bar for 10 days.

signature of superconductivity with an onset temperature (T_c^{onset}) of ≈7K emerges. With further compression, the T_c^{onset} gradually increases, reaching the maximum of ≈30K at 77.9 GPa in this study. The transport experiments of Crystal #2 were conducted under pressures ranging from 2.7 to 21.8 GPa (Figure 2f). The MMT and superconducting signature were successfully reproduced with similar T_{MMT} and T_c^{onset}, confirming the reproducibility and reliability of our results. Figure S11 (Supporting Information) shows the field dependence of the resistance of Crystal #1 at 57.9 GPa. It can be seen that T_c is significantly

Table 1. Experimental single-crystal structure details of $La_4Ni_3O_{10\text{-}\delta}$ structural solutions.

Pressure [GPa]	0.0001	5.7	11.0	16.6	25.7
Chemical formula	$La_4Ni_3O_{10}$	$La_4Ni_3O_{10}$	$La_4Ni_3O_{10}$	$La_4Ni_3O_{10}$	$La_4Ni_3O_{10}$
Wavelength (Å)	0.71073	0.3738	0.3738	0.3738	0.3738
M_r	891.77	891.77	891.77	891.77	891.77
Space group	$P2_1/a$	$P2_1/a$	*Bmab*	*I4/mmm*	*I4/mmm*
Unit cell	a = 5.4143(18) Å b = 5.4532(16)Å c = 14.220(5)Å β = 101.0(4)°	a = 5.3631(5) Å b = 5.3998(7) Å c = 14.1082(17) Å β = 101.2(12)°	a = 5.3229(9) Å b = 5.3282(9) Å c = 27.505(3) Å	a = 3.7345(6) Å b = 3.7345(6) Å c = 27.258(5) Å	a = 3.6891(14) Å b = 3.6891(14) Å c = 26.884(12) Å
V (Å^3)	412.13(2)	400.77(7)	780.08(2)	380.16(14)	365.9(3)
Z	2	2	4	2	2
No. of measured, independent and observed [I > 2σ(I)] reflections	6019 847 597	1171 819 697	615 326 223	349 220 203	184 128 73
R_{int}	0.052	0.010	0.011	0.019	0.191
$R[F^2 > 2\sigma(F^2)]$	0.048	0.0727	0.0533	0.042	0.070
$wR(F^2)$, *S*	0.135, 1.024	0.2016, 1.046	0.2155, 1.073	0.121, 1.03	0.173, 1.083
No. of parameters	80	79	50	25	25
$\Delta\rho_{max}$, $\Delta\rho_{min}$ (e Å^{-3})	1.93, −2.44	3.46, −4.90	2.38, −1.94	3.67, −3.54	2.80, −2.02

suppressed with an increasing magnetic field up to 9 T. By utilizing the criteria of 90% of the normal state resistance values, we extrapolated the value of upper critical magnetic field $\mu_0H_{c2}(T)$ at 57.9 GPa and zero temperature to be 24 T, and calculated the zero-temperature coherence length $\xi(0)$ to be 3.7 nm, using the Ginzburg-Landau (GL) model.[60,61]

PTM is critical for observation of a zero-resistance state under high pressure. There are two possible reasons why a zero-resistance state was not obtained in Crystal #1 and #2: (i) Oxygen deficiency. We have measured the oxygen content of $La_4Ni_3O_{10\text{-}\delta}$ polycrystalline powders annealed using the same conditions as Crystal #1 and #2 (annealed at 900 °C for 10 h in air) using TGA. An oxygen content of 9.95(2) and 10.00(1) was obtained from two different batches (Figure S10c,d, Supporting Information), indicating a near stoichiometry in Crystal #1 and #2. For stoichiometric $La_4Ni_3O_{10}$, superconductivity with a zero-resistance state at ~7K has been reported by Zhu et al.[32] Thus, we can exclude the possibility of oxygen deficiency in Crystal #1 and #2 as the reason for the lack of zero resistance. (ii) Inhomogeneity of PTM at high pressures. Indeed, superconductivity in $La_4Ni_3O_{10}$ has been reported by several papers;[32,33,54,62–65] however, zero resistance was obtained only using helium as PTM.[32,62,65] To the best of our knowledge, helium gas is the best PTM. The effects of PTM on nickelate superconductivity have also been discussed in bilayer $La_3Ni_2O_7$[66] and hybrid R-P $La_2NiO_4{\cdot}La_3Ni_2O_7$.[37]

2.4. Crystal Structure of Pressurized $La_4Ni_3O_{10\text{-}\delta}$ Single Crystals

To investigate the relationship between the emergence of superconductivity of $La_4Ni_3O_{10\text{-}\delta}$ and its crystal structure under high pressure, in situ synchrotron X-ray powder diffraction measurements were performed up to 22.5 GPa at room temperature using silicone oil as PTM (Figure S12a, Supporting Information). $La_4Ni_3O_{10\text{-}\delta}$ undergoes a pressure-induced structural transition at ≈ 9.3 GPa, as indicated by the clear variation in XRD peaks in the 2θ range of 12–19° (Figure S12b, Supporting Information). The pressure of this structural phase transition is lower compared with the value in the transport measurements at which the MMT disappears and superconductivity emerges. The crystal structure of $La_4Ni_3O_{10}$ under high pressure has been reported to be *I4/mmm* by Zhu et al.[32] and Li et al.[54] We thus refined our data using *I4/mmm*, and the results are reasonable (Figure S13 and Table S1, Supporting Information). Considering notably broad peaks, we also performed Rietveld refinements on our data using *Fmmm* and *Bmab*. It turns out that the refinements are also reasonable; however, the lengths of the two short axes do not merge, as expected for *I4/mmm* (Figure S13 and Table S1, Supporting Information). Our result suggests that there may exist an intermediate structure between ambient-pressure $P2_1/a$ and high-pressure *I4/mmm*. Therefore, within our resolution of powder diffraction, it is difficult to determine the crystal structure under high pressure.

We then move to SC-XRD on $La_4Ni_3O_{10\text{-}\delta}$. At ambient conditions, the reflections were indexed in a monoclinic system with lattice parameters: a = 5.4143(18) Å, b = 5.4532(16) Å, c = 14.220(5) Å, and β = 101.01(4)° (**Table 1**; Tables S2–S5, Supporting Information). Systematic absences of reflections with indices $h0l$: $h = 2n + 1$ and $0kl$: $k = 2n + 1$ suggest a primitive lattice with an a-glide plane and a 2_1 screw axis along the b-axis, confirming the space group of $P2_1/a$.[43] To investigate the structural evolution of $La_4Ni_3O_{10\text{-}\delta}$ under pressure, synchrotron SC-XRD measurements were performed at ID27 (λ = 0.3738 Å, ESRF) at pressures of 5.7, 11.0, 16.6, and 25.7 GPa. The crystal structures of $La_4Ni_3O_{10\text{-}\delta}$ are schematically presented in **Figure** 3a–c. At 5.7 GPa, the space group *Ccce* was initially assigned. However,

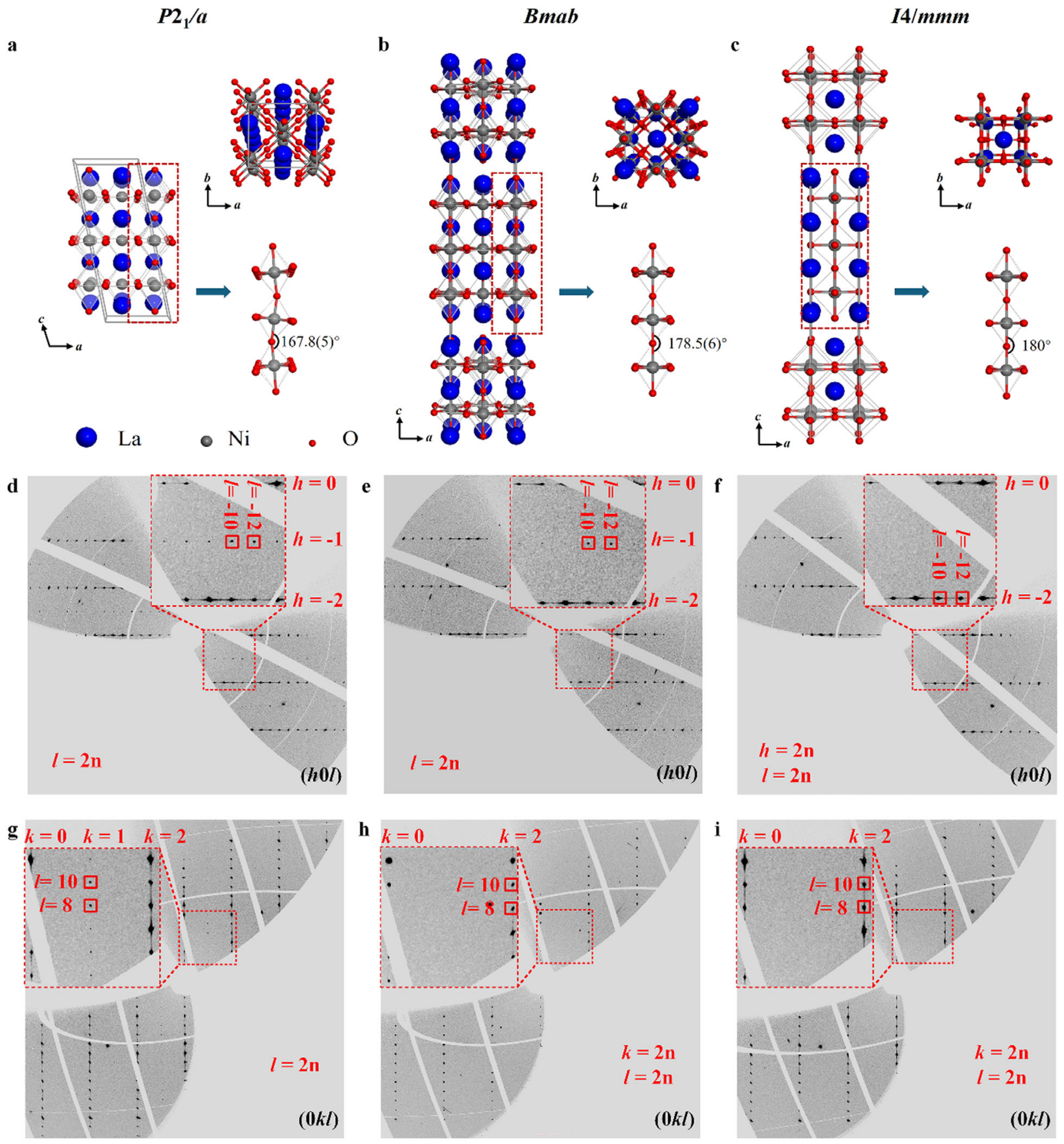

Figure 3. Pressure-induced structural transitions in $La_4Ni_3O_{10-\delta}$ single crystals. a) Monoclinic crystal structure at 5.7 GPa. b) Orthorhombic crystal structure at 11.0 GPa. c) Tetragonal crystal structure at 16.6 GPa. d,g) (*h*0*l*) and (0*kl*)-reciprocal planes reconstructed from single crystal X-ray diffraction data at 5.7 GPa. e,h) (*h*0*l*) and (0*kl*)-reciprocal planes reconstructed from single crystal X-ray diffraction data at 11.0 GPa. f,i) (*h*0*l*) and (0*kl*)-reciprocal plane reconstructed from single crystal X-ray diffraction data at 16.6 GPa. Note that for easy comparison the reciprocal planes shown in d–i are reconstructed using the orthorhombic setting of $a \approx 5.41$ Å, $b \approx 5.45$ Å, and $c \approx 27$ Å.

the presence of reflections with indices $h0l$ ($h + l = 2n + 1$) violates the extinction rule of a base-centered lattice (Figure 3d,g). Instead, the monoclinic space group $P2_1/a$, consistent with the ambient-pressure structure, was adopted. The refined lattice parameters at 5.7 GPa were $a = 5.3631(5)$ Å, $b = 5.3998(7)$ Å, $c = 14.1082(17)$ Å, and $\beta = 101.211(12)°$ (Table 1; Tables S6–S9, Supporting Information). Structural analysis revealed an overall compression, with a reduction in unit cell volume and a decrease in the separation between adjacent Ni-O layers. Within the NiO_6 octahedra, significant bond shortening was observed, with Ni-O distances contracting to 1.891–2.128 Å. At 11.0 GPa, systematic extinction of reflections with $k = 2n + 1$ in the $0kl$ reciprocal

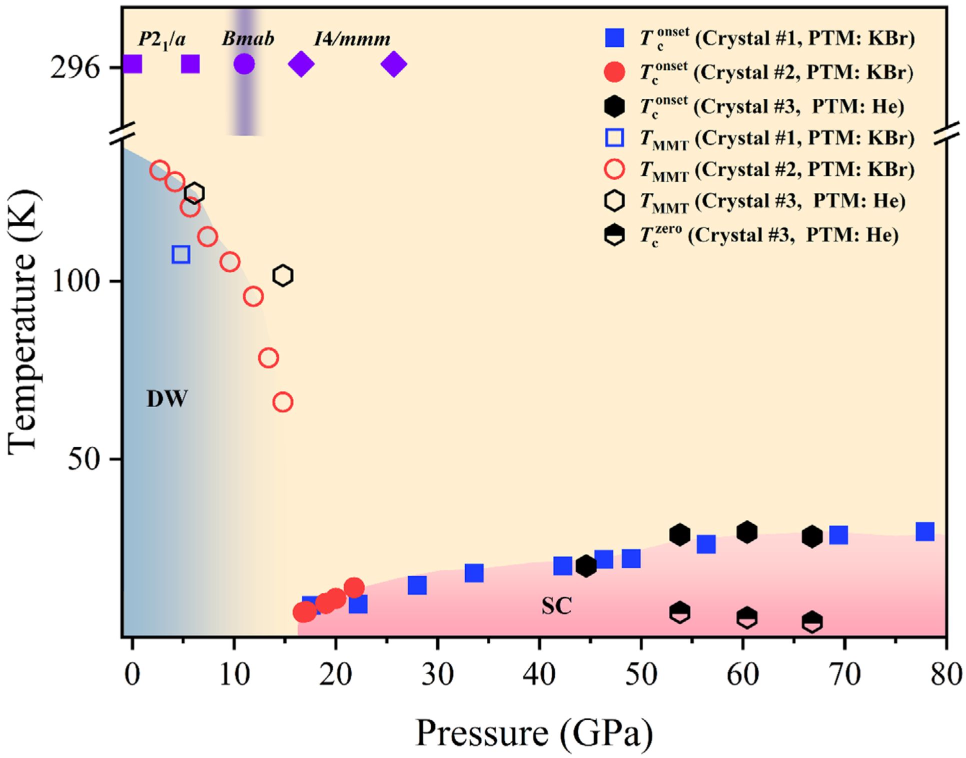

Figure 4. T-P phase diagram of $La_4Ni_3O_{10-\delta}$. The blue solid squares, the red solid circle, and the black solid hexagons represent the T_c^{onset} of Crystal #1, Crystal #2, and Crystal #3, respectively. The blue hollow squares, the red hollow circle, and the black hollow hexagons represent the T_{MMT} of Crystal #1, Crystal #2, and Crystal #3, respectively. The half solid and half hollow hexagon show T_c^{zero} of Crystal #3 at various pressures. The violet solid square, violet solid circle, and violet solid diamonds represent monoclinic $P2_1/a$, orthorhombic *Bmab* and tetragonal *I4/mmm*, respectively. Note that MMT is short for metal-to-metal transition, DW for density waves, and SC represents superconductivity. T_c^{onset} is defined as the temperature at which the resistance deviates from its linear dependence at high temperature. T_c^{zero} is defined as the temperature at which the resistance is zero. Crystal #1 and Crystal #2 were annealed at 900 °C in air for 10 h, and Crystal #3 was annealed at 600 °C under pO_2 = 1.5 bar for 10 days.

lattice plane indicated a pressure-induced symmetry transition (Figure 3e,h). The reflections were indexed in an orthorhombic system with lattice parameters of a = 5.3229(9) Å, b = 5.3282(9) Å, c = 27.505(3) Å (Table 1; Tables S10–S13, Supporting Information). The observed extinction conditions ($h0l$: $l = 2n + 1$ and $0kl$: $k, l = 2n + 1$) confirmed a base-centered cell with an a-glide plane along the c-axis. Based on maximization of symmetry and intensity statistics ($|E^2 - 1|$), the space group *Bmab* was selected for structural refinement. At this pressure, NiO_6 octahedra exhibited a substantial reduction in distortion, with Ni—O bond lengths becoming more uniform within the ab-plane. The out-of-plane Ni-O-Ni angle is 178.5(6)°, which is smaller deviating from 180° compared with that at 5.7 GPa. A further symmetry transition occurred at 16.6 GPa, evidenced by the extinction of reflections with $h = 2n + 1$ in the $h0l$ reciprocal lattice plane (Figure 3f,i). The structural transformation led to a body-centered tetragonal phase with space group *I4/mmm* and lattice parameters of a = 3.7345(6) Å, b = 3.7345(6) Å, c = 27.258(5) Å (Table 1; Tables S14–S17, Supporting Information). This transition was marked by complete geometric regularization of NiO_6 octahedra, as confirmed by bond-angle analysis, which indicated collinear alignment (180°) of octahedral connectivity both within the ab-plane and along the c-axis. At 25.7 GPa, further compression of the unit cell was observed, but no additional symmetry transitions occurred. The crystal structure remained in the *I4/mmm* symmetry (Table 1; Tables S18–S21, Supporting Information), suggesting that $La_4Ni_3O_{10-\delta}$ maintains a stable tetragonal phase under higher pressures. However, the degradation of crystallinity in $La_4Ni_3O_{10-\delta}$ resulted in diffraction data that were less precise for full refinement beyond 16.6 GPa.

2.5. *T-P* Phase Diagram of $La_4Ni_3O_{10-\delta}$

We summarized our high-pressure transport data and structural data in **Figure 4**. At ambient pressure, $La_4Ni_3O_{10-\delta}$ undergoes a MMT originating from intertwined charge and spin density waves,[59] which is gradually suppressed with increasing pressure. When pressure was increased to 25.7 GPa at room temperature, a cascade of structural transitions occurs from monoclinic $P2_1/a$ to orthorhombic *Bmab* to tetragonal *I4/mmm*. Superconductivity was observed after the crystal structure becomes *I4/mmm*, with a maximum T_c^{onset} of ≈30K and T_c^{zero} of 7K. Overall, our phase diagram is consistent with those of Zhu et al[32] and Zhang et al,[33] whose $La_4Ni_3O_{10}$ single crystals were prepared by floating zone growth at an oxygen pressure of 18–22 bar. Notably, there are two differences: (I) We identified an orthorhombic *Bmab* between ambient pressure $P2_1/a$ and high pressure *I4/mmm* via SC-XRD. Such a structure under high pressure was not reported previously. The out-of-plane Ni—O—Ni bond angle of 168.4(6)° in $P2_1/c$ at ambient pressure transformed into 178.5(6)° in *Bmab* at 11 GPa, and finally transformed into 180° in $I4/mmm$ at 16.6 GPa. The low-pressure monoclinic $P2_1/c$ and the intermediate *Bmab* structure with out-of-plane Ni-O-Ni angle of 168.4(6)°–178.5(6)° are non-superconducting under high pressure, while the tetragonal structure with out-of-plane Ni-O-Ni angle of 180° supports superconductivity. Our data indicate a strong correlation between out-of-plane Ni-O-Ni angle of 180° and the emergence of superconductivity under high pressure, offering fresh experimental evidence for understanding the superconducting mechanism in nickelates. (II) The pressures for disappearance of density waves and the emergence of superconductivity are slightly different. Density waves survive up to ≈15 GPa in our measurements, similar to Zhang et al.[33] and much higher than those of Zhu et al.[32] In addition, Zhu et al.[32] reported superconductivity at a pressure as low as 2.2 GPa, while Zhang et al.[33] found superconductivity at ≈ 10 GPa, which is pretty close to our observations. There are two possibilities for the above difference in critical pressures: (i) Inhomogeneity of pressure environment between different PTMs, and (ii) Subtle structural difference between single crystals grown using different methods. Although both single crystals grown from ambient-pressure flux method and high pO_2 floating zone growth techniques crystallize in the same monoclinic structure $P2_1/a$, their lattice parameters, bond lengths, and bond angles are slightly different (Table 1 vs Table 1 in Ref.[41]). Specifically, the averaged in-plane and out-of-plane Ni—O bond lengths of $La_4Ni_3O_{10-\delta}$ single crystals grown at ambient pressure are slightly shorter than those grown under high oxygen pressure (Figure S14, Supporting Information). In contrast, the out-of-plane Ni—O—Ni bond angle of $La_4Ni_3O_{10-\delta}$ crystals grown at ambient pressure is a bit larger than that of $La_4Ni_3O_{10-\delta}$ crystals grown under high oxygen pressure (Figure S14, Supporting Information).

3. Conclusion

We performed high-pressure electrical resistance measurements and high-pressure single-crystal X-ray diffraction on high-quality $La_4Ni_3O_{10-\delta}$ single crystals grown at ambient pressure. SC-XRD, NQR and STEM data demonstrate that our samples are long-range ordered single crystals with perfect stacking of trilayers. Electrical resistance measurements under high pressure show suppression of charge/spin density wave order and emergence of superconductivity. Superconductivity with the maximum T_c^{onset} of ≈30K and T_c^{zero} of 7K at 53.8 GPa was observed. When the pressure increases to 25.7 GPa at room temperature, a cascade of structural transitions occurs from monoclinic $P2_1/a$ to orthorhombic *Bmab* to tetragonal $I4/mmm$ based on synchrotron X-ray single crystal diffraction. Notably, the intermediate-pressure orthorhombic *Bmab* was not reported previously. Our data indicate a strong correlation between out-of-plane Ni-O-Ni angle of 180° and the emergence of superconductivity under high pressure, offering fresh experimental evidence for understanding the superconducting mechanism in nickelates. Finally, our successful observation of superconductivity with T_c^{onset} of ≈30K and T_c^{zero} of 7K in ambient-pressure grown single crystals of R-P nickelates completely removes the requirement of high oxygen pressure during crystal growth, which is expected to significantly advance the field of nickelate superconductivity research.

4. Experimental Section

Single Crystal Growth: All experiments were carried out at ambient pressure.[43] La_2O_3 (Sigma–Aldrich, 99.99%) was baked at 600 °C for 5 h before use. La_2O_3 and Ni (Alfa Aesar, 99.8%, particle size 5–15 µm) powders with molar ratio of 2:3 were weighed, mixed, and ground, and then placed in an Al_2O_3 crucible. The mixture was mixed with anhydrous K_2CO_3 powders which were used as a flux. The crucible was covered with a lid in order to minimize evaporation of K_2CO_3. Loading anhydrous K_2CO_3 was performed in a glove box and mixed and ground with La_2O_3 and Ni using a mortar.

In-House Powder X-Ray Diffraction (PXRD): Bruker AXS D2 Phaser powder X-ray diffractometer was used to check phase purity of pulverized single crystals. Data were collected at room temperature using Cu-K_α radiation ($\lambda = 1.5418$ Å) in the 2θ range of 10–140° with a scan step size of 0.01° and a scan time of 1.2 s per step. TOPAS 6 was used for Rietveld refinement. Refinement parameters include background (Chebyshev function, order 13), sample displacement, lattice parameters, and strain.

In-House SCXRD at Ambient Condition: SC-XRD data were collected on a Bruker AXS D8 Venture (Mo-$K_{\alpha 1}$ radiation, $\lambda = 0.71073$ Å) diffractometer at 298K. A single crystal with dimensions of 0.058 × 0.064 × 0.036 mm^3 was used for this experiment. Indexing was performed using Bruker APEX5 software.[67] Data integration and cell refinement were performed using SAINT, and multiscan absorption corrections were applied using the SADABS program.[67] Processing images were synthesized using APEX5.[67]

Electrical Resistivity at Ambient Pressure: The resistivity of $La_4Ni_3O_{10-\delta}$ was measured by a standard four-probe method. Because of the small size of single crystals, it is difficult to make four contacts on a single crystal, so resistivity was measured using polycrystalline bars. Pulverized single crystals of $La_4Ni_3O_{10-\delta}$ with 100 mg were weighed and pressed into thin pellets. It was then sintered at 900 °C in air for 10 h. This round slice was then cut into long rectangular bars to make electrodes with silver paste. Quantum Design MPMS3 SQUID magnetometer with the Electrical Transport Option (ETO) was used to measure resistivity in the temperature range of 1.8–300K at a warming rate of 2K min^{-1} under external magnetic fields of 0, 1, 3, 5, and 7 T.

Magnetic Susceptibility at Ambient Pressure: DC magnetic susceptibility was measured using a Quantum Design MPMS3 SQUID magnetometer. Pulverized single crystals of $La_4Ni_3O_{10-\delta}$ were pressed into thin sheets and then annealed at 900 °C in the air for 10 h. We then used a small amount of GE Varnish to attach the sheet to the quartz holder. ZFC-W (zero-field cooling with data collected on warming), FC-C (field cooling and data collected on cooling), and FC-W (field cooling and data collected on warming) data were collected between 1.8 and 300K under an external magnetic field of 0.5 T. After cooled to 1.8K under zero magnetic field, data were collected on warming at a rate of 3K min^{-1}. FC-C and FC-W data collection used the same rate of 3K min^{-1}. FC-C data were also collected under magnetic fields of 1, 3, 5, and 7 T.

Scanning Transmission Electron Microscopy (STEM): STEM specimens were prepared by crushing $La_4Ni_3O_{10-\delta}$ single crystals in ethanol. A drop of the suspensions was deposited on lacey carbon-coated molybdenum grids and dried in air. High-angle annular dark-field (HAADF)-STEM images were acquired at an accelerating voltage of 300 kV on a double-aberration-corrected transmission electron microscope (Spectra 300, Thermo Fisher Scientific), equipped with a field-emission electron source. The probe convergence semi-angle and inner collection semi-angle are 25.0 and 49.0 mrad, respectively.

Synchrotron X-Ray Powder Diffraction (PXRD) Measurements under High Pressure: Single-crystal $La_4Ni_3O_{10-\delta}$ samples were ground into powder and loaded into a chamber (diameter 100 µm) pre-indented using a Re gasket, which was assembled in a diamond anvil cell (DAC) with a culet diameter of 250 µm. Silicone oil was employed as the PTM. The pressures were determined by the fluorescence of ruby.[68] Room-temperature synchrotron PXRD data were collected by a focused monochromatic X-ray beam (2.5 × 3.5 μm^2) with a wavelength of $\lambda = 0.6199$ Å at BL15U1 in Shanghai Synchrotron Radiation Facility. A Mar165 CCD was used as the detector. The detector distance and other geometric parameters of the sample were calibrated using a CeO_2 standard. XRD images were integrated to 2D diffraction patterns by using the DIOPTAS program.[69] The full profile analyses of the diffraction patterns and the Rietveld refinements were conducted using GSAS-II packages.[70]

Synchrotron SC-XRD under High Pressure: Two independent experiments at room temperature were conducted to investigate the structural phase transition of $La_4Ni_3O_{10}$ under ambient and high-pressure conditions. In run 1, a black, block-shaped single crystal of $La_4Ni_3O_{10}$ (0.023 × 0.21 × 0.18 mm^3) was selected and mounted on the tip of a thin glass fiber. In run 2, two $La_4Ni_3O_{1n}$ crystal fragments (≈10 µm in diameter) were loaded into a DAC (200 µm culet diameter). A Re gasket, indented to a thickness of 30 µm with a 130 µm hole, where the samples were placed along with a ruby sphere and a piece of gold for pressure calibration.[68,71] Neon gas was used as the PTM. SC-XRD measurements in run 1 were performed using an in-house Bruker D8 VENTURE diffractometer (Mo Kα radiation, $\lambda = 0.7107$ Å). The beam diameter was ≈ 110 µm. High-pressure data collection followed the strategy described by Dawson et al.[72] with sample reflections manually harvested using the SMART software. Image masks were created using ECLIPSE[73] to exclude detector regions obscured by the DAC. Data integration and oblique correction were performed with SAINT,[67] and absorption effects were corrected using the Multi-Scan method (SADABS).[67] High-pressure SC-XRD measurements in run 2 were conducted at the ID27 beamline of the ESRF ($\lambda = 0.3738$ Å), with a beam diameter of approximately 2 µm.[74] At each pressure step, data were collected in step-scans of 0.5° while rotating the DAC from −35° to +35° about the vertical axis (ω-scan). Single-crystal data analysis, including peak search, unit cell determination, and data integration, was performed using the CrysAlis^{Pro} software.[75] The crystal structures obtained from both experiments were determined using SHELXT and refined with SHELXL.[67]

Electrical Resistance Measurements under High Pressure using KBr as PTM: The diamonds had culets with a diameter of 300–500 µm, and sample chambers were drilled into a diameter of 120–200 µm. Insulating gaskets were prepared with a T301 stainless steel outer circumference coated with fine alumina powder mixed with epoxy as an insulator. The pressures were determined by the frequency shift of the diamond Raman edge.[76] The resistances were all measured via the four-probe van der Pauw method using four Pt electrodes with currents of 100 µA. KBr was employed as PTM. The temperature dependence of the electrical resistance was measured upon cooling and warming cycles with a slow temperature ratio (0.1K min^{-1}). The data were taken upon warming as it yields a more accurate temperature reading. Cu-Be alloy DACs were used for transport measurements under external magnetic fields up to 9 T.

Electrical Resistance Measurements under High Pressure using He as PTM: High-pressure resistance curves of $La_4Ni_3O_{10\text{-}\delta}$ single crystals were systematically investigated using a diamond anvil cell (DAC) configuration. Pressure calibration was performed at room temperature via ruby fluorescence shift. Transport property measurements were conducted on a Physical Properties Measurement System (PPMS-9, Quantum Design Inc.), with high-pressure resistivity characterization implemented in the DAC via the standard van der Pauw four-probe technique. The DAC utilized a 200 µm culet, and the sample chamber - fabricated from a cubic boron nitride-epoxy composite - featured a diameter of 100 µm to accommodate the single crystal specimen, which was loaded under helium pressure-transmitting conditions.

Nuclear Quadrupole Resonance (NQR): NQR measurements were conducted using a phase-coherent pulsed NQR spectrometer. ^{139}La-NQR spectra were obtained by sweeping the frequency point by point, and integrating spin-echo intensity. The quantity of $La_4Ni_3O_{10}$ single crystal samples used for NQR measurement is ≈ 60 mg.

Thermogravimetric Analysis (TGA): TGA of $La_4Ni_3O_{10\text{-}\delta}$ samples was carried out under 4% H_2/Ar atmosphere with the flow rate of 50 mL min^{-1} on a Mettler-Toledo TGA/DSC^{3+} instrument. Prior to samples test, five blanks were run in order to gain a good reference and very small mass fluctuation range of ≈10 µg. The measurement started from 100 °C, held for 1 h, followed by heating to 900 °C with a heating rate of 8K min^{-1} and held for 1 h to make sure the complete decomposition, and then cooled to room temperature. Finally, the oxygen content was determined by calculating the mass loss.

Supporting Information

Supporting Information is available from the Wiley Online Library or from the author.

Acknowledgements

Work at Shandong University was supported by the National Natural Science Foundation of China (Grant Nos. 12374457 and 12074219). G.L. was supported by the National Natural Science Foundation of China (Grant No. 12474010). Q.Z. was supported by the National Key Basic Research Program of China under Grant No. 2021YFA1202801. H.G. acknowledges funding support from the National Science Fund for Distinguished Young Scholars (Grant No. T2225027). Work at the Institute of Physics, Chinese Academy of Sciences was supported by the National Key Basic Research Program of China (Grant Nos. 2023YFA1406103 and 2024YFA1611302) and the National Natural Science Foundation of China (Grant Nos. 12374142, 12304170, and U23A6003). Q.S.Z. and D.P. acknowledge the support from Shanghai Key Laboratory of Material Frontiers Research in Extreme Environments, China (Grant No. 22dz2260800), and the Shanghai Science and Technology Committee, China (Grant No. 22JC1410300). J.Z. is grateful to Prof. Xutang Tao from Shandong University for providing valuable support. J.Z. thanks Dr. Yu-Sheng Chen and Dr. Tieyan Chang from The University of Chicago for stimulating discussions. J.Z. thanks Prof. Jinguang Cheng from the Institute of Physics Chinese Academy of Sciences for early collaboration on high pressure measurement. The authors also thank the European Synchrotron Radiation Facility for the provision of beamtime at the ID27 beamline (proposal HC-5923). A portion of this work was carried out at the Synergetic Extreme Condition User Facility (SECUF, https://cstr.cn/31123.02.SECUF). A portion of this research used resources at the beamline 15U1 of Shanghai synchrotron radiation facility.

Conflict of Interest

The authors declare no conflict of interest.

Author Contributions

J.Z. conceived the project and coordinated the experiments. F.L., Y.H., N.G., D.J., J.D., and D.P. contributed equally to this work. F.L. performed single crystal growth, X-ray powder diffraction, transport measurements, and magnetic susceptibility measurements with the help of J.Z. F.L. conducted in-house single crystal X-ray diffraction with the help of J.Z. and Jian Z. Y.H., L.X., G.L. conducted the electrical resistance measurements under high pressure using KBr as pressure transmitting medium. Y.H. and G.L. carried out the synchrotron X-ray powder diffraction experiments using silicone oil as pressure transmitting medium. N.G. and Q.Z. performed the scanning transmission electron microscopy measurements. D.J., W.Z., Y.H., X.W., Z.G., M.M., J.F.S.R., and H.G. performed single crystal X-ray diffraction experiments under high pressure. J.D., J.L., J.Y., and R.Z. carried out the nuclear quadrupole resonance experiments. D.P. and Q.S.Z. carried out high-pressure transport measurements using helium as pressure transmitting medium. F.L., Y.H., N.G., D.J., J.D., G.L., and J.Z. wrote the manuscript with contributions from all authors. All authors have discussed the results and the interpretations.

Data Availability Statement

The data that support the findings of this study are available in the supplementary material of this article.

Keywords

crystal structure, flux method, high-pressure superconductivity, nickelates, Ruddlesden-Popper phase, single crystal diffraction, Superconductivity

Received: April 17, 2025
Revised: July 28, 2025
Published online: August 22, 2025

---

[1] B. Keimer, S. A. Kivelson, M. R. Norman, S. Uchida, J. Zaanen, *Nature* **2015**, *518*, 179.

[2] S. Sanders, 125 Questions: Exploration and Discovery, Science, **2021**, p. 23.

[3] M. R. Norman, *Rep. Prog. Phys.* **2016**, *79*, 074502.

[4] J. G. Bednorz, K. A. Müller, *Rev. Mod. Phys.* **1988**, *60*, 585.

[5] P. Lacorre, *J. Solid State Chem.* **1992**, *97*, 495.

[6] V. I. Anisimov, D. Bukhvalov, T. M. Rice, *Phys. Rev. B* **1999**, *59*, 7901.

[7] J. Zhang, A. S. Botana, J. W. Freeland, D. Phelan, H. Zheng, V. Pardo, M. R. Norman, J. F. Mitchell, *Nat. Phys.* **2017**, *13*, 864.

[8] D. Li, K. Lee, B. Y. Wang, M. Osada, S. Crossley, H. R. Lee, Y. Cui, Y. Hikita, H. Y. Hwang, *Nature* **2019**, *572*, 624.

[9] B. Y. Wang, K. Lee, B. H. Goodge, *Annu. Rev. Condens. Matter Phys.* **2024**, *15*, 305.

[10] L. E. Chow, A. Ariando, *Front. Phys.* **2022**, *10*, 834658.

[11] Q. Gu, H.-H. Wen, *The Innovation* **2022**, *3*, 100202.

[12] Y. Nomura, R. Arita, *Rep. Prog. Phys.* **2022**, *85*, 052501.

[13] X. Zhou, P. Qin, Z. Feng, H. Yan, X. Wang, H. Chen, Z. Meng, Z. Liu, *Mater. Today* **2022**, *55*, 170.

[14] M. Hepting, M. P. M. Dean, W.-S. Lee, *Front. Phys.* **2021**, *9*, 808683.

[15] Y. Ji, J. Liu, L. Li, Z. Liao, *J. Appl. Phys.* **2021**, *130*, 060901.

[16] M. Osada, B. Y. Wang, K. Lee, D. Li, H. Y. Hwang, *Phys. Rev. Mater.* **2020**, *4*, 121801.

[17] M. Osada, B. Y. Wang, B. H. Goodge, S. P. Harvey, K. Lee, D. Li, L. F. Kourkoutis, H. Y. Hwang, *Adv. Mater.* **2021**, *33*, 2104083.

[18] S. Zeng, C. Li, L. E. Chow, Y. Cao, Z. Zhang, C. S. Tang, X. Yin, Z. S. Lim, J. Hu, P. Yang, A. Ariando, *Sci. Adv.* **2022**, *8*, -eabl9927.

[19] W. Wei, D. Vu, Z. Zhang, F. J. Walker, C. H. Ahn, *Sci. Adv.* **2023**, *9*, eadh3327.

[20] S. L. E. Chow, Z. Y. Luo, A. Ariando, *Nature* **2025**, *642*, 58.

[21] H. Sahib, A. Raji, F. Rosa, G. Merzoni, G. Ghiringhelli, M. Salluzzo, A. Gloter, N. Viart, D. Preziosi, *Adv. Mater.* **2025**, *37*, 2416187.

[22] C. T. Parzyck, Y. Wu, L. Bhatt, M. Kang, Z. Arthur, T. M. Pedersen, R. Sutarto, S. Fan, J. Pelliciari, V. Bisogni, G. Herranz, A. B. Georgescu, D. G. Hawthorn, L. F. Kourkoutis, D. A. Muller, D. G. Schlom, K. M. Shen, *Phys. Rev. X* **2025**, *15*, 021048.

[23] G. A. Pan, D. Ferenc Segedin, H. LaBollita, Q. Song, E. M. Nica, B. H. Goodge, A. T. Pierce, S. Doyle, S. Novakov, D. Córdova Carrizales, A. T. N'Diaye, P. Shafer, H. Paik, J. T. Heron, J. A. Mason, A. Yacoby, L. F. Kourkoutis, O. Erten, C. M. Brooks, A. S. Botana, J. A. Mundy, *Nat. Mater.* **2022**, *21*, 160.

[24] X. Yan, H. Zheng, Y. Li, H. Cao, D. P. Phelan, H. Zheng, Z. Zhang, H. Hong, G. Wang, Y. Liu, A. Bhattacharya, H. Zhou, D. D. Fong, *Sci. Adv.* **2025**, *11*, eado4572.

[25] Q. Li, C. He, J. Si, X. Zhu, Y. Zhang, H.-H. Wen, *Commun. Mater.* **2020**, *1*, 16.

[26] B.-X. Wang, H. Zheng, E. Krivyakina, O. Chmaissem, P. P. Lopes, J. W. Lynn, L. C. Gallington, Y. Ren, S. Rosenkranz, J. F. Mitchell, D. Phelan, *Phys. Rev. Mater.* **2020**, *4*, 084409.

[27] P. Puphal, Y.-M. Wu, K. Fürsich, H. Lee, M. Pakdaman, J. A. N. Bruin, J. Nuss, Y. E. Suyolcu, P. A. van Aken, B. Keimer, M. Isobe, M. Hepting, *Sci. Adv.* **2021**, *7*, eabl8091.

[28] H. Sun, M. Huo, X. Hu, J. Li, Z. Liu, Y. Han, L. Tang, Z. Mao, P. Yang, B. Wang, J. Cheng, D.-X. Yao, G.-M. Zhang, M. Wang, *Nature* **2023**, *621*, 493.

[29] G. Wang, N. Wang, X. Shen, J. Hou, L. Ma, L. Shi, Z. Ren, Y. D. Gu, H. M. Ma, P. T. Yang, Z. Y. Liu, H. Z. Guo, J. Sun, G. M. Zhang, S. Calder, J.-Q. Yan, B. Wang, Y. Uwatoko, J. G. Cheng, *Phys. Rev. X* **2024**, *14*, 011040.

[30] Y. Zhang, D. Su, Y. Huang, Z. Shan, H. Sun, M. Huo, K. Ye, J. Zhang, Z. Yang, Y. Xu, Y. Su, R. Li, M. Smidman, M. Wang, L. Jiao, H. Yuan, *Nat. Phys.* **2024**, *20*, 1269.

[31] N. Wang, G. Wang, X. Shen, J. Hou, J. Luo, X. Ma, H. Yang, L. Shi, J. Dou, J. Feng, J. Yang, Y. Shi, Z. Ren, H. Ma, P. Yang, Z. Liu, Y. Liu, H. Zhang, X. Dong, Y. Wang, K. Jiang, J. Hu, S. Nagasaki, K. Kitagawa, S. Calder, J.-Q Yan, J. Sun, B. Wang, R. Zhou, Y. Uwatoko, J. G. Cheng, *Nature* **2024**, *634*, 579.

[32] Y. Zhu, D. Peng, E. Zhang, B. Pan, X. Chen, L. Chen, H. Ren, F. Liu, Y. Hao, N. Li, Z. Xing, F. Lan, J. Han, J. Wang, D. Jia, H. Wo, Y. Gu, Y. Gu, L. Ji, W. Wang, H. Gou, Y. Shen, T. Ying, X. Chen, W. Yang, H. Cao, C. Zheng, Q. Zeng, J.-G. Guo, J. Zhao, *Nature* **2024**, *631*, 531.

[33] M. Zhang, C. Pei, D. Peng, X. Du, W. Hu, Y. Cao, Q. Wang, J. Wu, Y. Li, H. Liu, C. Wen, J. Song, Y. Zhao, C. Li, W. Cao, S. Zhu, Q. Zhang, N. Yu, P. Cheng, L. Zhang, Z. Li, J. Zhao, Y. Chen, C. Jin, H. Guo, C. Wu, F. Yang, Q. Zeng, S. Yan, L. Yang, Y. Qi, *Phys. Rev. X* **2025**, *15*, 021005.

[34] E. Zhang, D. Peng, Y. Zhu, L. Chen, B. Cui, X. Wang, W. Wang, Q. Zeng, J. Zhao, *Phys. Rev. X* **2025**, *15*, 021008.

[35] X. Chen, E. H. T. Poldi, S. Huyan, R. Chapai, H. Zheng, S. L. Bud'ko, U. Welp, P. C. Canfield, R. J. Hemley, J. F. Mitchell, D. Phelan, *Phys. Rev. B* **2025**, *111*, 094525.

[36] F. Li, N. Guo, Q. Zheng, Y. Shen, S. Wang, Q. Cui, C. Liu, S. Wang, X. Tao, G.-M. Zhang, J. Zhang, *Phys. Rev. Mater.* **2024**, *8*, 053401.

[37] M. Shi, D. Peng, K. Fan, Z. Xing, S. Yang, Y. Wang, H. Li, R. Wu, M. Du, B. Ge, Z. Zeng, Q. Zeng, J. Ying, T. Wu, X. Chen, *arxiv 2502.01018* **2025**.

[38] F. Li, Z. Xing, D. Peng, J. Dou, N. Guo, L. Ma, Y. Zhang, L. Wang, J. Luo, J. Yang, J. Zhang, T. Chang, Y.-S. Chen, W. Cai, J. G. Cheng, Y. Wang, Z. Zeng, Q. Zheng, R. Zhou, Q. Zeng, X. Tao, J. Zhang, *arxiv 2501.14584* **2025**.

[39] L. Wang, Y. Li, S.-Y. Xie, F. Liu, H. Sun, C. Huang, Y. Gao, T. Nakagawa, B. Fu, B. Dong, Z. Cao, R. Yu, S. I. Kawaguchi, H. Kadobayashi, M. Wang, C. Jin, H.-K. Mao, H. Liu, *J. Am. Chem. Soc.* **2024**, *146*, 7506.

[40] M. Shi, D. Peng, Y. Li, Z. Xing, Y. Wang, K. Fan, H. Li, R. Wu, Z. Zeng, Q. Zeng, J. Ying, T. Wu, X. Chen, arXiv 2501.14202, **2025**.

[41] J. Zhang, H. Zheng, Y. u.-S. Chen, Y. Ren, M. Yonemura, A. Huq, J. F. Mitchell, *Phys. Rev. Mater.* **2020**, *4*, 083402.

[42] M. Wang, H.-H. Wen, T. Wu, D.-X. Yao, T. Xiang, *Chin. Phys. Lett.* **2024**, *41*, 077402.

[43] F. Li, S. Wang, C. Ma, X. Wang, C. Liu, C. Fan, L. u. Han, S. Wang, X. Tao, J. Zhang, *Cryst. Growth Des.* **2024**, *24*, 347.

[44] E. K. Ko, Y. Yu, Y. Liu, L. Bhatt, J. Li, V. Thampy, C.-T. Kuo, B. Y. Wang, Y. Lee, K. Lee, J.-S. Lee, B. H. Goodge, D. A. Muller, H. Y. Hwang, *Nature* **2024**, *638*, 935.

[45] G. Zhou, W. Lv, H. Wang, Z. Nie, Y. Chen, Y. Li, H. Huang, W.-Q. Chen, Y.-J. Sun, Q.-K. Xue, Z. Chen, *Nature* **2025**, *640*, 641.

[46] V. Christiansson, F. Petocchi, P. Werner, *Phys. Rev. Lett.* **2023**, *131*, 206501.

[47] Y.-B. Liu, J.-W. Mei, F. Ye, W.-Q. Chen, F. Yang, *Phys. Rev. Lett.* **2023**, *131*, 236002.

[48] Z. Luo, X. Hu, M. Wang, W. Wú, D.-X. Yao, *Phys. Rev. Lett.* **2023**, *131*, 126001.
[49] R. Jiang, J. Hou, Z. Fan, Z.-J. Lang, W. Ku, *Phys. Rev. Lett.* **2024**, *132*, 126503.
[50] X.-Z. Qu, D.-W. Qu, J. Chen, C. Wu, F. Yang, W. Li, G. Su, *Phys. Rev. Lett.* **2024**, *132*, 036502.
[51] H. Sakakibara, N. Kitamine, M. Ochi, K. Kuroki, *Phys. Rev. Lett.* **2024**, *132*, 106002.
[52] Y. Zhang, L.-F. Lin, A. Moreo, T. A. Maier, E. Dagotto, *Nat. Commun.* **2024**, *15*, 2470.
[53] C. Xia, H. Liu, S. Zhou, H. Chen, *Nat. Commun.* **2025**, *16*, 1054.
[54] J. Li, C.-Q. Chen, C. Huang, Y. Han, M. Huo, X. Huang, P. Ma, Z. Qiu, J. Chen, X. Hu, L. Chen, T. Xie, B. Shen, H. Sun, D.-X. Yao, M. Wang, *Sci. China-Phys. Mech. Astron.* **2024**, *67*, 117403.
[55] C. Pei, M. Zhang, D. Peng, S. Huangfu, S. Zhu, Q. Wang, J. Wu, Z. Xing, L. Zhang, Y. Chen, J. Zhao, W. Yang, H. Suo, H. Guo, Q. Zeng, Y. Qi, arXiv 2411.08677, **2024**.
[56] X. Chen, J. Zhang, A. S. Thind, S. Sharma, H. LaBollita, G. Peterson, H. Zheng, D. P. Phelan, A. S. Botana, R. F. Klie, J. F. Mitchell, *J. Am. Chem. Soc.* **2024**, *146*, 3640.
[57] P. Puphal, P. Reiss, N. Enderlein, Y.-M. Wu, G. Khaliullin, V. Sundaramurthy, T. Priessnitz, M. Knauft, A. Suthar, L. Richter, M. Isobe, P. A. van Aken, H. Takagi, B. Keimer, Y. E. Suyolcu, B. Wehinger, P. Hansmann, M. Hepting, *Phys. Rev. Lett.* **2024**, *133*, 146002.
[58] H. Z. Wang, L. Chen, A. Rutherford, H. D. Zhou, W. W. Xie, *Inorg. Chem.* **2024**, *63*, 5020.
[59] J. Zhang, D. Phelan, A. S. Botana, Y.-S. Chen, H. Zheng, M. Krogstad, S. G. Wang, Y. Qiu, J. A. Rodriguez-Rivera, R. Osborn, S. Rosenkranz, M. R. Norman, J. F. Mitchell, *Nat. Commun.* **2020**, *11*, 6003.
[60] L. D. Landau, V. L. Ginzburg, *Zh. Eksp. Teor. Fiz.* **1950**, *20*, 1064.
[61] J. A. Woollam, R. B. Somoano, P. O'Connor, *Phys. Rev. Lett.* **1974**, *32*, 712.
[62] D. Peng, Y. Bian, Z. Xing, L. Chen, J. Cai, T. Luo, F. Lan, Y. Liu, Y. Zhu, E. Zhang, Z. Wang, Y. Sun, Y. Wang, X. Wang, C. Wang, Y. Yang, Y. Yang, H. Dong, H. Lou, Z. Zeng, Z. Zeng, M. Tian, J. Zhao, Q. Zeng, J. Zhang, H. Mao, *arXiv 2502.14410* **2025**.
[63] H. Sakakibara, M. Ochi, H. Nagata, Y. Ueki, H. Sakurai, R. Matsumoto, K. Terashima, K. Hirose, H. Ohta, M. Kato, Y. Takano, K. Kuroki, *Phys. Rev. B* **2024**, *109*, 144511.
[64] Q. Li, Y.-J. Zhang, Z.-N. Xiang, Y. Zhang, X. Zhu, H.-H. Wen, *Chin. Phys. Lett.* **2024**, *41*, 017401.
[65] M. Shi, Y. Li, Y. Wang, D. Peng, S. Yang, H. Li, K. Fan, K. Jiang, J. He, Q. Zeng, D. Song, B. Ge, Z. Xiang, Z. Wang, J. Ying, T. Wu, X. Chen, *Nat. Commun.* **2025**, *16*, 2887.
[66] J. Hou, P.-T. Yang, Z.-Y. Liu, J.-Y. Li, P.-F. Shan, L. Ma, G. Wang, N.-N. Wang, H.-Z. Guo, J.-P. Sun, Y. Uwatoko, M. Wang, G.-M. Zhang, B.-S. Wang, J.-G. Cheng, *Chin. Phys. Lett.* **2023**, *40*, 117302.
[67] Bruker, APEX Software, Bruker Analytical X-ray Instruments, Inc. V5, Bruker, Germany, **2023**.
[68] H. K. Mao, J. Xu, P. M. Bell, *J. Geophys. Res. Solid Earth* **1986**, *91*, 4673.
[69] C. Prescher, V. B. Prakapenka, *High Pressure Res.* **2015**, *35*, 223.
[70] B. H. Toby, R. B. Von Dreele, *J. Appl. Crystallogr.* **2013**, *46*, 544.
[71] M. Yokoo, N. Kawai, K. G. Nakamura, K.-I. Kondo, Y. Tange, T. Tsuchiya, *Phys. Rev. B* **2009**, *80*, 104114.
[72] A. Dawson, D. R. Allan, S. Parsons, M. Ruf, *J. Appl. Crystallogr.* **2004**, *37*, 410.
[73] S. Parsons, ECLIPSE – Program for masking high pressure diffraction images and conversion between CCD image formats. Department of Chemistry, University of Edinburgh, Edinburgh, UK, **2010**.
[74] M. Mezouar, G. Garbarino, S. Bauchau, W. Morgenroth, K. Martel, S. Petitdemange, P. Got, C. Clavel, A. Moyne, H.-P. Van Der Kleij, A. Pakhomova, B. Wehinger, M. Gerin, T. Poreba, L. Canet, A. Rosa, A. Forestier, G. Weck, F. Datchi, M. Wilke, S. Jahn, D. Andrault, L. Libon, L. Pennacchioni, G. Kovalskii, M. Herrmann, D. Laniel, H. Bureau, *High Pressure Res.* **2024**, *44*, 171.
[75] Rigaku, *CrysAlis*$^{\text{PRO}}$ - Single crystal X-ray diffraction dta collection and processing software, Rigaku Oxford Diffraction Ltd., Oxford, UK, **2015**.
[76] A. Yuichi, K. Haruki, *J. Phys.: Conf. Ser.* **2010**, *215*, 012195.